Seismic detection of meteorite impacts on Mars

N.A. Teanby, J. Wookey

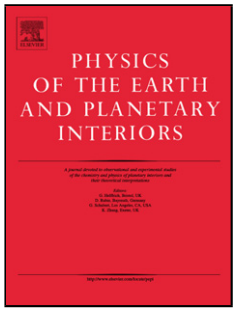

Title: Seismic detection of meteorite impacts on Mars

Authors: N.A. Teanby, J. Wookey

PII: S0031-9201(11)00056-2
DOI: doi:10.1016/j.pepi.2011.03.004
Reference: PEPI 5388

To appear in: *Physics of the Earth and Planetary Interiors*

Received date: 24-7-2010
Revised date: 3-3-2011
Accepted date: 9-3-2011

Please cite this article as: Teanby, N.A., Wookey, J., Seismic detection of meteorite impacts on Mars, *Physics of the Earth and Planetary Interiors* (2010), doi:10.1016/j.pepi.2011.03.004

-We model seismic signals generated by meteorite impacts on Mars.
-We predict the total seismic moment released by impacts is 1e13-1e14Nm per year.
-Nominally, about one globally detectable impact event should occur every ten years.
-Meteorite impacts do not provide a dependable way of probing the deep interior.

Seismic detection of meteorite impacts on Mars

N. A. Teanby[a], J. Wookey[a]

[a]*Department of Earth Sciences, University of Bristol, Wills Memorial Building, Queen's Road, Bristol, BS8 1RJ, UK.*

Abstract

Meteorite impacts provide a potentially important seismic source for probing Mars' interior. It has recently been shown that new craters can be detected from orbit using high resolution imaging, which means the location of any impact-related seismic event could be accurately determined - thus improving the constraints that could be placed on internal structure using a single seismic station. This is not true of other seismic sources on Mars such as sub-surface faulting, which require location using multiple seismic stations. This study aims to determine the seismic detectability of meteorite impacts and assess whether they are a viable means of probing deep internal structure. First, we derive a relation between crater diameter and equivalent seismic moment based on observational data compiled from impact tests, controlled explosions, and earthquake seismology. Second, this relation was combined with updated cratering rates based on newly observed craters to derive the impact induced seismicity on Mars, which we estimate to total 10^{13}–10^{14} Nm per year. Finally, seismic waveform modelling was used to determine the detectability of these impacts based on reasonable assumptions about likely seismometer performance and background noise levels. For our

Email address: n.teanby@bristol.ac.uk (N. A. Teanby)

nominal noise/instrument case we find that detectable impacts at teleseismic distances (source-receiver offsets greater than 60°) are very rare and occur approximately once every 10 years. For our most optimistic noise/instrument case, approximately one such event occurs each year. This suggests that using solely meteorite impacts is not a reliable way of probing the Martian interior, although local impacts are more frequently detectable and could provide important constraints on near surface seismic properties.

Keywords: Mars, Seismology, Internal Structure, Planets.

1. Introduction

The major geophysical tools for probing planetary interiors are seismology, geomagnetism, observed orbital changes of planetary satellites, and measurements of the gravitational field and moment of inertia. Internal models can also be predicted using geochemical modelling based on the composition of representative meteorites. On Earth, seismology provides the most detailed information on internal structure and has been used to determine core and mantle structure (e.g. Dziewonski and Anderson, 1981). Further properties can be determined by measurements of the global magnetic field, especially the state of the conducting inner and outer cores.

Mars has no internal magnetic field (Acuna et al., 1999; Connerney et al., 1999) or reliable seismic data so currently the only way to estimate internal structure is to develop models that are consistent with the measured moment of inertia of $I=0.365MR^2$ (Yoder et al., 2003; Sohl et al., 2005) and an assumed composition based on SNC meteorites, which are believed to be representative of the bulk Martian composition (Sohl and Spohn, 1997). Many

different interior models can fit these constraints and as a result, basic properties remain relatively unconstrained. The size of the core is uncertain and there are currently at least three suggested core models with various combinations of solid and liquid cores (e.g. Stevenson, 2001). The composition and velocity structure of the core and mantle are also poorly constrained.

The best way to improve our knowledge of Mars' interior is with a global seismic network. However, off-Earth seismology is extremely challenging. The seismometer must survive the rigours of launch, landing, and harsh environments with large temperature swings. Another challenge is remote deployment onto the planet surface in a way that provides good seismic coupling. The Apollo seismic experiment, deployed by astronauts, detected numerous seismic events on the Moon, and has revolutionised our understanding of the lunar interior. Internal models now exist for lunar density (Bills and Ferrari, 1977), velocity structure (Goins et al., 1981; Nakamura, 1983; Khan et al., 2000; Lognonne et al., 2003; Gagnepain-Beyneix et al., 2006; Khan et al., 2007), and seismic attenuation (Nakamura, 1976; Goins et al., 1981; Nakamura and Koyama, 1982).

On Mars, the Viking seismometer (Anderson et al., 1976) was badly affected by wind noise due to its position on the lander and poor coupling to the ground, but was able to place crude upper limits on Mars' current activity. Anderson et al. (1976) suggest that the Viking seismometer would require a magnitude 6.5-7.0 event to be globally detectable (equivalent seismic moment 10^{19}–10^{20} Nm), whereas Goins and Lazarewicz (1979) suggest a magnitude as high as 9.0-10.0 would be required. However, subsequent research has predicted current activity should be well below these levels.

Possible sources of seismicity on Mars include: (1) Fracturing caused by thermal and lithostatic stresses predicted from visible faults in high resolution images and topographic data (Golombek et al., 1992; Knapmeyer et al., 2006). These authors predict total yearly moment releases of 10^{18} Nm and 3×10^{16}–5×10^{18} Nm respectively, occurring mostly as small sub-magnitude 5 events; (2) Volcanic events, for which there is evidence of recent (<50Ma) activity from crater counting. Sub-surface events are most likely as no current surface activity is observable; and (3) Meteorite impacts, which based on extrapolation of Apollo lunar data should be detectable (Davis, 1993). On Earth, the majority of seismic events are due to plate tectonics - a process that appears to be long since dormant on Mars - but which may have operated in Mars' early history prior to 3.5Ga (Sleep, 1994).

Although Mars is much less seismically active than the Earth, the background noise is also expected to be orders of magnitude lower, due to the thin atmosphere coupled with the absence of major terrestrial noise sources such as ocean waves, anthropogenic sources, and lack of vegetation for coupling wind noise into the subsurface. Therefore, a seismic investigation of the Martian interior should be possible with a low noise - well coupled instrument network.

Both ESA and NASA are considering deployment of seismic instrumentation on Mars in the near future. Mission scenarios have included both broad-band and short-period instruments (Lognonne et al., 1996, 2000; Pike et al., 2005). Although Mars is predicted to be seismically active, this has not yet been confirmed with seismic instruments. Therefore, the initial goal of such a mission would be to determine the level and global distribution of

current Martian seismic activity. This is a key measurement for determining both the level of further seismic exploration and the ability of seismology to address the major goal of constraining Mars' internal structure.

Through model refinement by comparison with the observed phases a single seismic station would provide some new constraints on Mars' interior. However, such analysis will require many assumptions and accurate location of the seismic source would require triangulation from at least three or four well spaced stations (Mocquet, 1999). This is especially true for stress related faulting and sub-surface volcanism, for which the source location would be unknown. However, Malin et al. (2006) recently showed that it is possible to detect new meteorite impact sites on Mars - with 20 new impact craters catalogued over a seven year period. Therefore, if a similar standard of impact monitoring could be achieved during a seismic experiment, event location would be accurately known (to within meters, depending on the instrument pixel size) and the constraints we could place on Mars' interior would be greatly improved.

Impacts of meteors and projectiles have been detected on the Moon by the Apollo seismometers and suggest that seismic detection would be possible (Oberst and Nakamura, 1987; Latham et al., 1970a,b). Davis (1993) extrapolated the Apollo results to Mars and concluded that meteorites may indeed act as a very effective seismic source, with around 20 globally detectable impacts occurring per year. However, the Moon is thought to be seismically very different to Mars with low velocity zones, low seismic attenuation, and significant sub-surface scattering. This leads to non-conventional waveforms comprising very long wave trains with extended P and S-wave

coda (Lognonne, 2005). The Moon also has no atmosphere, and lies in a different gravitational environment to Mars so the meteorite flux is expected to be very different. Davis (1993) tried to take many of these factors into account, but never-the-less, extrapolating the lunar results to Mars introduces a large degree of uncertainty.

In this paper we use new craters observed by Malin et al. (2006) to remove as many assumptions as possible, and directly model wave propagation through Mars' interior using a representative seismic model. From this we estimate the number of observable meteorite impacts per year given estimates of seismometer sensitivity and Martian background noise.

2. Mars' Meteorite Induced Seismicity

Comparison of recent high resolution imaging of Mars from Mars Global Surveyor (MGS) over a seven year period has resulted in the detection of 20 new impact craters with diameters ranging from 2 to 148 m (Malin et al., 2006). If we can determine the relation between observed crater size and the impact equivalent seismic moment for Mars then these observations can be used to determine the frequency of impacts with a particular moment. This defines the meteorite induced seismicity and determines how many meteorite strikes could be detectable in a given observation period. This should provide a more reliable estimate of meteorite detectability than scaling the Apollo seismic data.

To determine the seismicity we must consider four things: (1) The current impact rate on Mars for a given crater size. (2) The relation between observed crater sizes and impact energy. (3) The efficiency of conversion of impact

energy into seismic wave energy. (4) The relationship between seismic energy and an equivalent seismic moment. Each of these factors is now considered in turn in order to derive an overall relation between crater diameter and seismic moment.

2.1. Current Impact Rate on Mars

Hartmann (2005) presents the latest chronology of Mars' cratering history. Assuming this chronology and that the cratering rate has been approximately constant for the last 3 Gyrs gives the 1-year isochron shown Figure 1. However, considerable uncertainty exists in the small crater diameter (<1 km) regime and Hartmann (2005) quotes a factor of 3 uncertainty.

The 20 new craters observed by Malin et al. (2006) can be used to reduce this uncertainty and validate/adjust the chronology of Hartmann (2005) in this uncertain region. However, as discussed by Hartmann (2007) it should be noted that: (1) the frequency of occurrence of the smallest crater sizes observed by Malin et al. (2006) should be regarded as a lower limit, as the detection limit of their image analysis was around 10 m diameter; and (2) the largest new crater (148 m) was much larger than any of the other craters observed and is probably not representative of the time averaged meteorite flux.

Figure 1 compares the Malin et al. (2006) MGS results to the isochron of Hartmann (2005). The agreement is impressive considering the gross extrapolation required to get from the 3 Gyr to 1 year isochron. However, the MGS results suggest less cratering than predicted, and we find that the best fit to the observations is obtained by scaling the Hartmann (2005) isochrons by 1/3 (if craters <10 m and the 148 m crater are ignored). This is also

consistent with Quantin et al. (2007), who suggest a factor of 3 reduction in impact rates over the last 3 Gyrs.

The Hartmann (2005) isochrons include a reduction in smaller impact events caused by atmospheric ablation and fragmentation effects discussed by Popova et al. (2003), who found that below 4 m the possibility of crater formation is heavily dependent on meteorite composition. Hence, we do not consider craters under 4 m diameter, as these will be difficult to detect from orbit and have a large uncertainty in flux.

2.2. Crater Diameter-Impactor Energy Dependence

Cratering mechanisms are reviewed in detail by Melosh (1980, 1989), and more recently by Richardson et al. (2005) and Holsapple and Housen (2007) motivated by the Deep Impact mission. Here, we are concerned with the relation between impactor kinetic energy E and the resulting crater diameter D. It is found that the relationship between these quantities can be well represented by empirically derived scaling laws (Horedt and Neukum, 1984). These generally take the form of a power law $D = aE^b$, where a and b are constants with b varying between 1/4 and 1/3 depending on experimental conditions. More complex relationships can also be derived, which include secondary effects such as target/impactor material properties and impact angle (Holsapple and Schmidt, 1982; Horedt and Neukum, 1984).

For our study we only have one observable to describe the meteorite impact with Mars - the crater diameter. Therefore, we only aim to determine one parameter - the impact energy E, which is the most important factor determining crater diameter. To this end we use the cratering database of Holsapple et al. (2003), which covers laboratory drop tests, high energy

impact studies, and craters formed by conventional and nuclear detonations prior to 1998. We augmented this database by including additional studies and recently published data for: explosions (Nordyke, 1962; Goto et al., 2001; Ambrosini et al., 2002); impacts (Schmidt and Housen, 1987); and drop tests (Barnouin-Jha et al., 2007). To fill in the higher energy regime we also include a study of volcanic caldera diameters (Sato and Taniguchi, 1997).

The resulting database contains information on crater diameters for a large range of source energies, types, and incidence angles with target materials ranging from water and ice through to rocks and metals. From this database we selected experimental data for non-metal solids (rock, sand, coral, and alluvium) at standard Terrestrial conditions (1 bar pressure and 1 g gravitational acceleration). Many of the test explosions were either buried at significant depth or detonated above ground. To ensure that the measurements were relevant to meteorite impacts we only included explosions where the ratio of source depth to final crater diameter was in the range -0.05 to 0.2. These limits were chosen because typically impact craters have a depth of one fifth of their diameter, so an explosion with a depth-diameter ratio of 0.2 or less should still be representative of an impact, whereas the small negative value of -0.05 was chosen so as to include explosives that were detonated just above the surface for experimental reasons (on a short rig/mount for example), but gave crater sizes indistinguishable from surface explosions. The equivalent source depth for the volcanic calderas is unknown, but they appear to follow the same scaling as the higher energy explosions so we also included these points.

Figure 2 shows energy versus crater diameter for our subset of the database.

Data from selected individual studies are also plotted for comparison and to show the scatter that occurs even under relatively uniform experimental conditions. A standard unit of energy for many of the older studies was equivalent pounds of TNT (lbs TNT) for small explosions or kilo-ton yields for nuclear detonations. We have converted these units into Joules using 1 lb TNT = 1.90 MJ and 1 kilo-ton = 4.18 TJ (Shoemaker, 1983) and included them as a secondary axes for ease of comparison.

Despite energy variations over 10 orders of magnitude, the dependence of crater diameter on energy is remarkably linear - especially over the D = 2–148 m range, which is our region of primary interest as it corresponds to the new craters detected from orbit by Malin et al. (2006). There is a discrepancy for very low impact energy drop tests, where crater forming processes appear more efficient. However, such low energy events are not relevant for our study as ablation by Mars' atmosphere prevents the formation of craters smaller than 0.3 m (Popova et al., 2003). Explosion and impact generated craters give consistent results, which is fortunate as it is not possible to perform controlled impact studies with energy much over 10^9 J and chemical/nuclear explosive analogues must be used.

To determine the scaling relation we fitted a straight line to the E-D data in log-log space using robust estimation to minimise the absolute deviation (L1-norm) between model and data (Press et al., 1992). This method is less susceptible to outliers than the more usual least squares L2-norm minimisation. Only measurements with energies greater than 10^5 J were used to create the line of best fit (corresponding to craters over 0.3 m diameter). Our

resulting scaling law for craters under Terrestrial conditions is given by:

$$D = 8.8^{+2.6}_{-3.5} \times 10^{-3} E^{0.32 \pm 0.01} \quad (1)$$

where D is in meters and E is in Joules. The error bars on the constant of proportionality were chosen such that the minimum/maximum range encompassed 68% of the measured datapoints. The error bars on the power are formal 1-σ errors from the robust fit. Unknown factors relating to the impact conditions, such as impact angle and rock properties, are included in our overall error estimate, which provides a measure of the uncertainty in determining the impactor energy from crater diameter alone.

The gravity on Mars is 3.73 ms^{-2} compared to 9.81 ms^{-2} on Earth. Because lower gravity makes craters easier to excavate, this will result in slightly larger craters than predicted by the above scaling law, which was derived for Terrestrial conditions. However, compared to other factors and scatter in the data, this effect is relatively small. Horedt and Neukum (1984) review the early literature and suggest that gravity affects the crater diameter by a factor of $(g_\oplus/g)^{3/16}$, where g and $g_\oplus$ are the surface gravity on the planet and on Earth respectively. This value is consistent with the impact of Ranger 8 on the lunar surface, which resulted in a crater approximately 13 m across (Whitaker, 1972), compared to the expected 9.5 m from missile impacts with similar materials and trajectories at the White Sands missile range in Nevada (Moore and Baldwin, 1968). The Deep Impact crater may provide additional insight on gravity scaling under very low gravity conditions but at present the crater diameter is hard to determine (Busko et al., 2007).

Therefore, our overall scaling law for a general planet - including uncertainty for unknown source/target parameters and a gravity correction - is

given in SI units (D in meters, E in Joules, and g in ms^{-2}) by:

$$D = 8.8^{+2.6}_{-3.5} \times 10^{-3} E^{0.32\pm0.01} \left(\frac{g_{\oplus}}{g} \right)^{3/16} \quad (2)$$

This compares well with the diameters of artificial impact craters created by Ranger 7–9 and Apollo 13 and 14 booster impacts measured from Apollo 16 (Whitaker, 1972).

2.3. Seismic Efficiency - k

Only a small fraction of a meteorite's kinetic energy goes into creating seismic waves. The bulk of the energy is expended as heat during deformation of the target along with the energy used to excavate the crater. The fraction of the total impact energy E converted into seismic energy E_s is known as the seismic efficiency k, which can be derived experimentally using impacts or explosive analogues. Combining k with the cratering rate and impact energy to crater diameter scaling law will allow us to determine the number of seismic events with a given energy.

Compiled experimental data from laboratory impact tests (McGarr et al., 1969), missiles impacts (Latham et al., 1970b), lunar module ascent stage (LM) and the Apollo 13 third stage Saturn booster (S-IVB) lunar impacts (Latham et al., 1970a), surface detonated nuclear explosions (Pomeroy, 1963), and underground nuclear detonations (Patton and Walter, 1993) are shown in Figure 3. The results of numerical calculations by Walker (2003) are also shown for comparison. Note that underground nuclear explosions are much more efficient at coupling seismic energy into the ground and have high seismic efficiencies of around 0.2-4$\times10^{-2}$. However, these efficiencies are not representative of surface impacts.

The experimental data suggest a seismic efficiency in the range k=10^{-4}–10^{-6}. For comparison, Chyba et al. (1998) adopted a value of k=10^{-4} for the Earth, Davis (1993) used k=10^{-6} for Mars, and Lognonne et al. (2009) used k=10^{-5} in a recent study of lunar impacts. The value of k=10^{-4} is closer to the values calculated by Walker (2003), however, these calculations show a trend for decreasing k as the impact energy increases, suggesting that lower values are appropriate for our energy range of interest (E >10^{11}J).

We adopt a value of k=2×10^{-5}, in keeping with the high energy results. However, this value contains considerable uncertainty. The experimental conditions for the lower k values may also not be an accurate representation of what happens during a high energy impact event. For example, the value from Pomeroy (1963) was obtained from a 5 Mton nuclear device detonated on a shallow water barge over a Pacific atoll, which provided sub-optimal conditions for the creation of seismic waves. Therefore, our value of k=2×10^{-5} most probably represents a conservative estimate and must include a large factor of 10 error.

2.4. Relation Between Seismic Moment and Seismic Energy

In order to calculate synthetic seismograms we require the equivalent seismic moment of the source. Therefore, we need to know how the seismic moment M is related to the seismic energy E_s. We can then use the seismic efficiency and impact energy to calculate M for a particular impact event.

Seismic energy is difficult to determine experimentally as attenuation in the Earth's crust preferentially removes high frequencies, which contain most of the energy. This has lead to some controversy in determining the relation between M and E_s, which is discussed by Shearer (2009).

Ide and Beroza (2001) compiled data from six studies: from micro-earthquakes to teleseismic events and concluded that the relation $E_s = 3 \times 10^{-5} M$ fits the data very well, although there is a large amount of scatter about this mean value (the bulk of the data lies in the range $E_s/M = 10^{-6}$ to 10^{-4}).

However, the attenuation problem means that seismic energy estimation from teleseismic events is very difficult, so the studies of small local earthquakes may be more representative. They also cover the range of energies of interest for our study. Figure 4 shows a compilation of three large studies where seismic energy and moment were determined. A robust (L1 norm) fit to this dataset yields the relation:

$$E_s = 4.8^{+2.9}_{-1.8} \times 10^{-9} M^{1.24 \pm 0.01} \quad (3)$$

Error bars are 1-σ, E_s is in Joules, and M is in Nm. The results from the impact modelling by Walker (2003) (assuming $k = 2 \times 10^{-5}$) and nuclear explosions by Patton and Walter (1993) are also shown. These are in broad agreement with both trends. However, the $E_s = 4.8 \times 10^{-9} M^{1.24}$ relation provides a better overall fit to the data in this energy range and is the one we use here.

2.5. Overall Relation Between Crater Diameter and Seismic Moment

To summarise the results of the previous sections, we have considered the following key variables: impact energy E in Joules; crater diameter D in meters; dimensionless seismic efficiency k; seismic energy E_s in Joules; and seismic moment M in Nm. These quantities are related by:

$$D = a E^b \left(\frac{g_\oplus}{g} \right)^{3/16} \quad (4)$$

$$E_s = kE \quad (5)$$

$$E_s = cM^d \quad (6)$$

Our observed quantity is D and we require the equivalent seismic moment M, which is given by the overall relation:

$$M(D) = \left(\frac{D}{a}\right)^{\frac{1}{bd}} \left(\frac{k}{c}\right)^{\frac{1}{d}} \left(\frac{g}{g_\oplus}\right)^{\frac{3}{16bd}} \quad (7)$$

The values of the constants and their fractional errors are given in Table 1. This table also gives the contribution of each of the uncertainties to the overall fractional error in M for a given observed D using the error propagation equations in Bevington and Robinson (1992). The overall fractional error in our estimate of M is of order $\sigma_M/M \approx 8$. Therefore, there is around an order of magnitude uncertainty in seismic moment for a given impact event.

Table 2 summarises our results for the impact induced seismicity of Mars and gives the number of impact events with a given D and M in each decadal energy bin, with the impact rates determined from the modified Hartmann (2005) isochrons. The seismic moment magnitude M_w, defined by $M_w = 2/3(\log_{10} M - 9.1)$ (Kanamori, 1977), is also given for ease of comparison with terrestrial events.

3. Mars Interior Model

Current knowledge of Mars' interior is reviewed by Lognonne (2005). Here we are concerned with velocity, density, and seismic attenuation as these determine how seismic waves propagate throughout the interior.

3.1. Velocity Structure

Early models of Mars' interior are summarised by Okal and Anderson (1978). More recently, Sohl and Spohn (1997) presented two end-member models of Mars' velocity and density structure, such that either the fit to SNC meteorite bulk composition or the observed moment of inertia was optimised. As a representative model, we adopt model A from Sohl and Spohn (1997) (optimised to fit the observed moment of inertia), which is plotted in Figure 5.

3.1.1. Seismic Attenuation: Q

Seismic attenuation is parameterised by the quality factor Q. Obviously, this is a significant unknown at seismic frequencies for Mars. However, it can be estimated at long periods (∼20000s) from measurements of the secular acceleration of Phobos and extrapolated to seismic frequencies. Zharkov and Gudkova (1997) determined the mean dissipative factors at tidal frequencies, and using a five-layer density model and uniform Q model inferred values of Q_s=177 assuming a solid core and Q_s=261 assuming a liquid core for periods of 1s. Yoder et al. (2003) show Mars has a liquid core, so we assume Q_s=261 throughout Mars' interior. Q_p is assumed to be $2.25Q_s$ following standard relations (e.g. Shearer, 2009). This yields an attenuation value which is similar to the average for the upper 2000 km Earth's mantle (where Q_s =280). Without structural information we cannot constrain depth dependence. However, the attenuation is a path-integral effect so a uniform value for the Martian mantle is sufficient for our purposes.

4. Seismic Source Function

The seismic frequency content of the source will depend on the impact energy. Larger events will have more energy concentrated at lower frequencies. Here, we assume a simple displacement source function $S(f)$ after Boatwright (1980) as used by Abercrombie (1995).

$$\frac{S(f)}{S_0} = \frac{1}{(1+(f/f_c)^{\gamma n})^{1/\gamma}} \quad (8)$$

where f is frequency, f_c is the corner frequency, S_0 is a reference displacement at long period, γ=2, and n=2. This model gives a source spectra that falls in between those for an idealised fault (Brune, 1970), which has slightly less high frequency content, and that for an underground nuclear explosion (Mueller and Murphy, 1971), which has slightly higher frequency content. All three models tend to a classic f^{-2} dependence at high frequency.

The corner frequency f_c has a weak dependence on the source moment M, such that $f_c \propto M^{-1/3}$ (Shearer, 2009). For micro-earthquakes the relation is given approximately by:

$$f_c = 2 \times 10^5 M^{-1/3} \quad (9)$$

which was derived using the corner frequencies determined from high sample rate measurements of micro-earthquakes by Abercrombie (1995). Figure 6 shows the source spectra using Equations 8 and 9 for a range of seismic moments.

Note that for all but the largest events, the source spectrum is flat until relatively high frequencies and will have limited effect on the seismogram

frequency content compared to seismic attenuation in the crust and mantle. Therefore, for most impacts a delta function in displacement would provide an excellent approximation to the source.

5. Synthetic Seismograms

Synthetic Martian seismograms were generated using the direct solution method (DSM) (Geller and Ohminato, 1994; Geller and Takeuchi, 1995; Takeuchi et al., 1996), which allows generation of accurate full waveform synthetics at global scales.

During high energy/high velocity impacts, such as a meteorite impacting a planet, the impactor tends to fragment and vapourise. This leads to the creation of radially symmetric craters for all but the steepest impact angles. Therefore, the most appropriate seismic source is a purely isotropic (explosive) source (Stein and Wysession, 2002), defined by the moment tensor:

$$\mathbf{M_T} = \begin{pmatrix} M_{11} & 0 & 0 \\ 0 & M_{22} & 0 \\ 0 & 0 & M_{33} \end{pmatrix} \tag{10}$$

where $M_{11} = M_{22} = M_{33}$. The scalar seismic moment M is then defined by:

$$M = \frac{1}{\sqrt{2}} \left(\sum_{i=1}^{3} \sum_{j=1}^{3} M_{ij}^2 \right)^{\frac{1}{2}} \tag{11}$$

which reduces to $M = \sqrt{3/2} M_{11}$ in our case.

Modelling shallow events is too computationally expensive (Kawai et al., 2006), but is only required for surface wave generation. In this study we are only interested in body waves amplitudes, as these waves sound the deep

interior. Body wave amplitudes are affected very little by changing the model source depth (Figure 7), so for our purposes accurate impact-generated body waves can be modelled using a shallow source at 50 km depth.

Models were run at 1, 2, 4, and 8 Hz maximum frequency using a 64000 gridpoint vertical velocity model and spherical harmonics up to degree 64000 to give a model spatial resolution of around 50 m, which gave 10 times oversampling of the shortest wavelength seismic waves. The 8 Hz synthetics took 48khr equivalent CPU time. Computation time scaled as the cube of frequency, so it was not computationally practical to model frequencies higher than 8 Hz. Although the DSM method calculates the full wavefield, in the following we only analyse P waves. These are expected to be the most energetic phase for non-shear sources like impacts and so represent the best chance for probing the interior.

Figure 8 shows waveforms calculated for each maximum modelled frequency for three source-receiver offsets. If waveforms are not modelled with a high enough maximum frequency then "ringing" effects will be seen around the arrivals and the amplitudes of the waveforms will not have converged. Comparison of synthetics with different maximum frequencies was used to check for amplitude convergence. Due to seismic attenuation, it was not necessary to model frequencies higher than 8 Hz to accurately model synthetic seismograms with offsets over 30°. However, closer seismograms travel shorter distances and have been attenuated less. Therefore, at close range higher maximum frequency is required. These effects are just visible in the 20° offset synthetics in Figure 8, which have not quite fully converged. Therefore, amplitudes at offsets less than 20° will be underestimated, but as we are

primarily concerned with teleseismic events (as these provide information on the deep structure) this does not pose a problem for our analysis.

The seismic displacement source function from Section 4 was applied to the synthetics although this had negligible effect compared to seismic attenuation for events with $M \leq 10^{14}$ Nm.

Figure 9 shows a record section obtained from our modelling. Travel time curves of the various phases were calculated by ray tracing using the Tau-p toolkit (Crotwell et al., 1999) and are overlain for comparison. On Mars the P-wave shadow zone starts at around 110° offset.

Figure 10 shows the frequency content of the P-wave envelope as a function of source-receiver offset angle. Seismic attenuation limits the frequency content of teleseismic arrivals within the 0.4–4 Hz band. More distant arrivals are attenuated more and have a lower frequency content. Note that for Earth, accurate seismograms can be obtained using a maximum modelled frequency of 2 Hz (Kawai et al., 2006). However, the smaller radius of Mars requires modelling to higher frequencies (4–8 Hz) as there is less distance for the seismic waves to be attenuated and the frequency content is thus higher.

6. Results

Figure 11 shows the maximum P-wave amplitude as a function of epicentral distance for a range of impact equivalent source moments after band pass filtering with a 0.4–4 Hz 16 pole Butterworth filter. The difference between the 1, 2, 4, and 8 Hz maximum frequency models again shows that for close events with offsets less than 20° the amplitudes have not quite fully converged and should be regarded as lower limits. These predicted amplitudes can be

compared to expected background noise levels and instrument sensitivities to determine how many events would be likely to be detected per year.

The major noise source on Mars is likely to be induced by winds. Lognonne et al. (1996) calculated a conservative estimate of the wind induced noise spectral density of 10^{-9} $ms^{-2}Hz^{-1/2}$. For comparison, on Earth the noise spectral density in our frequency range of interest (0.4-4 hz) is around 3×10^{-9} $ms^{-2}Hz^{-1/2}$ for a low noise site if the ocean wave-induced microseismic noise peak at 0.2 Hz is ignored (Peterson, 1993). Mars should be much quieter than the Earth and a noise spectral density of 10^{-10} $ms^{-2}Hz^{-1/2}$ is not unreasonable for a wind-shielded instrument or during calm meteorological periods (e.g. night time).

The instrumental noise of typical terrestrial broad band seismometers (Nanometrics Trillium240, Guralp CMG3T, and Streckeisen STS2) range from 0.5–5×10^{-10} $ms^{-2}Hz^{-1/2}$ at 1 Hz. For Mars, a very broad band seismometer developed at IPGP in France has a noise level approaching 10^{-10} $ms^{-2}Hz^{-1/2}$ at 1 Hz (Lognonne et al., 2000). Another approach would be to use an extended frequency range micro-seismometer, such as the micro-machined silicon instrument under development for planetary applications by Pike et al. (2005). This seismometer is predicted to have a noise level of around 1–3×10^{-8} $ms^{-2}Hz^{-1/2}$ at 1 Hz, although further improvements in performance may be possible.

Therefore, to cover the range of likely background and instrument noise levels we consider three rms noise spectral densities: 10^{-10} $ms^{-2}Hz^{-1/2}$, 10^{-9} $ms^{-2}Hz^{-1/2}$, and 10^{-8} $ms^{-2}Hz^{-1/2}$. The lowest noise would correspond to a high specification broad band instrument under quiet condi-

tions, whereas the highest noise case represents an exploration-class instrument in a non-ideal deployment. These noise spectral densities n_{rms} were converted into maximum peak acceleration a_{peak} using the formula $a_{peak} = 1.25 n_{rms} \sqrt{(f_2 - f_1)}$, where f_1–f_2 is the frequency range under consideration (Havskov and Alguacil, 2004).

Under nominal noise conditions (10^{-9} ms^{-2}Hz$^{-1/2}$) Figure 11 shows that to detect an event at teleseismic distances (offset $\Delta \geq 60°$) requires a seismic moment over 10^{13} Nm (M_w=2.6), or equivalently an impact producing a 100 m diameter or larger crater. From Table 2 such large craters are produced every 1–8 years or 4 years on average. A globally detectable event would require a moment of around 10^{14} Nm (M_w=3.3).

Figure 12 summarises the number of detectable impacts for each noise level in each of the decadal energy bins in Table 2. The number of detectable impacts at a given site per year per energy bin N_e is given by:

$$N_e = \frac{(1 - \cos\theta)}{2} i_e \tag{12}$$

where i_e is the number of impacts per year over the whole of Mars in each energy bin, θ is the maximum offset at which an event is detectable, and the $(1 - \cos\theta)/2$ factor gives the fractional surface area of Mars over which an event would be detectable. The nominal noise case represents the most likely scenario and shows that a single seismic station would detect impacts with $\Delta \geq 60°$ approximately once every 10 years. For the low noise case, which assumes a more sensitive instrument, around one such event occurs per year.

7. Discussion and Conclusions

In this paper we derive a relation between crater diameter and equivalent seismic moment for meteorite impacts. This is important for accurate modelling of the seismic signals produced by impacts. When combined with the impact rate determined from crater counting and recently observed new craters, synthetic seismograms can be modelled using a representative Mars internal model and used to predict the number of seismically detectable impacts per year.

Our seismic modelling shows that a detectable event requires a seismic moment of at least 10^{13} Nm to be detected above the predicted noise level at teleseismic distances ($\Delta \geq 60°$) and a moment of 10^{14} Nm to be detected globally. These figures are consistent with a previous study by Mocquet (1999).

Our study suggests that globally detectable impact events on Mars are very rare and most probably do not provide a dependable way of probing the deep interior. Nominal assumptions about noise and seismic parameters suggest only one impact at $\Delta \geq 60°$ is detectable every 10 years. If low noise conditions are assumed, detection of one such event per year is predicted. If in addition to low noise, we are very optimistic and use the more favourable end-members of the likely seismic parameter space, detections for offsets $\Delta \geq 60°$ could be as high as 10 per year per site. However, based on current understanding of impact processes we regard this as unlikely.

Therefore, our estimates of meteorite detectability are much less than those of Davis (1993), who applied scaling to the lunar results and predicted around 20 globally detectable impact events per year. The main reason for

this discrepancy is the downward revision of the Martian impactor flux over the last decade or so. Comparing our Table 2 to Table III of Davis (1993) shows that we predict about two orders of magnitude less events for a given energy.

The seismicity due to impactors can be compared to that from shallow surface and lithospheric faulting estimated from faults observed on Mars' surface with high resolution imagery and topography measurements. By summing the product of the impact equivalent seismic moments and impact rates in Table 2, we estimate the total seismic moment release per year due to impacts to be 10^{13}–10^{14} Nm. Golombek et al. (1992) estimated that around 50 globally detectable ($M > 10^{14}$ Nm) faulting events should occur per year, with a total yearly moment release of 10^{18} Nm. A more recent analysis by Knapmeyer et al. (2006) predicts a yearly moment release from faults in the range 3×10^{16}–5×10^{18} Nm, with around 100 $M > 10^{14}$ Nm events (depending on the fault model used). Therefore, these studies suggest that faulting induced seismicity should be a much more effective way to probe the Martian interior than meteorite impacts. However, this leaves us with the problem of locating the events, which would require measurements at multiple stations.

This paper shows that seismic waves generated by meteorite impacts probably cannot be relied upon for sounding the interior of Mars. If low noise and optimistic seismic parameters are assumed around 10 teleseismic range impacts could be detectable per year. However, using our nominal noise and parameter values predicts only one detectable teleseismic range impact every 10 years. Seismic efficiency and background noise levels are

the most poorly understood or our seismic parameters and introduce considerable uncertainty into the detection rates. Due to the large uncertainty, impacts should not be ruled out as a means for probing Mars' interior, but are expected to be of secondary importance to faulting. Local impacts will be more detectable and occur more often - providing valuable constraints on near-surface properties - but are less well suited to probing the deep interior. However, if even one global impact event could be seismically detected and the crater identified, this would provide some of the best constraints we have so far on Mars' interior structure.

8. Acknowledgements

This research is supported by the Science and Technology Facilities Council and the European Research Council. We thank Renee Weber and an anonymous reviewer for valuable comments and suggestions on the manuscript.

References

Abercrombie, R. E., 1995. Earthquake source scaling relationships from -1 to 5 M_L using seismograms recorded at 2.5-km depth. J. Geophys. Res. B100, 24015–24036.

Acuna, M. H., Connerney, J. E. P., Ness, N. F., Lin, R. P., Mitchell, D., Carlson, C. W., McFadden, J., Anderson, K. A., Reme, H., Mazelle, C., Vignes, D., Wasilewski, P., Cloutier, P., 1999. Global distribution of crustal magnetization discovered by the Mars Global Surveyor MAG/ER experiment. Science 284, 790–793.

Ambrosini, R. D., Luccioni, B. M., Danesi, R. F., Riera, J. D., Rocha, M. M., 2002. Size of craters produced by explosive charges on or above the ground surface. Shock Waves 12, 69–78.

Anderson, D. L., Duennebier, F. K., Latham, G. V., Toksoz, M. F., Kovach, R. L., Knight, T. C. D., Lazarewicz, A. R., Miller, W. F., Nakamura, Y., Sutton, G., 1976. Viking seismic experiment. Science 194, 1318–1321.

Barnouin-Jha, O. S., Yamamoto, S., Toriumi, T., Sugita, S., Matsui, T., 2007. Non-intrusive measurements of crater growth. Icarus 188, 506–521.

Bevington, P. R., Robinson, D. K., 1992. Data reduction and error analysis for the physical sciences, 2nd Edition. WBC/McGraw-Hill, New York.

Bills, B. G., Ferrari, A. J., 1977. Lunar density model consistent with topographic, gravitational, librational, and seismic data. J. Geophys. Res. 82, 1306–1314.

Boatwright, J., 1980. A spectral theory for circular seismic sources - simple estimates of source dimension, dynamic stress drop, and radiated seismic energy. Bull. Seism. Soc. Am. 70, 1–27.

Brune, J. N., 1970. Tectonic stress and spectra of seismic shear waves from earthquakes. J. Geophys. Res. 75, 4997–5009.

Busko, I., Lindler, D., A'Hearn, M. F., White, R. L., 2007. Searching for the Deep Impact crater on comet 9P/Tempel 1 using image processing techniques. Icarus 187, 56–68.

Chyba, C. F., van der Vink, G. E., Hennet, C. B., 1998. Monitoring the comprehensive test ban treaty: Possible ambiguities due to meteorite impacts. Geophys. Res. Lett. 25, 191–194.

Connerney, J. E. P., Acuna, M. H., Wasilewski, P. J., Ness, N. F., Reme, H., Mazelle, C., Vignes, D., Lin, R. P., Mitchell, D. L., Cloutier, P. A., 1999. Magnetic lineations in the ancient crust of Mars. Science 284, 794–798.

Crotwell, H. P., Owens, T. J., Ritsema, J., 1999. The TauP Toolkit: Flexible seismic travel-time and ray-path utilities. Seis. Res. Lett. 70, 154–160.

Davis, P. M., 1993. Meteoroid impacts as seismic sources on Mars. Icarus 105, 469–478.

Dziewonski, A. M., Anderson, D. L., 1981. Preliminary reference earth model. Phys. Earth Planet. Int. 25, 297–356.

Gagnepain-Beyneix, J., Lognonne, P., Chenet, H., Lombardi, D., Spohn, T., 2006. A seismic model of the Lunar mantle and constraints on temperature and mineralogy. Phys. Earth Planet. Int. 159, 140–166.

Geller, R. J., Ohminato, T., 1994. Computation of synthetic seismograms and their partial derivatives for heterogeneous media with arbitrary natural boundary-conditions using the direct solution method. Geophys. J. Int. 116, 421–446.

Geller, R. J., Takeuchi, N., 1995. A new method for computing highly accurate DSM synthetic seismograms. Geophys. J. Int. 123, 449–470.

595 Goins, N. R., Dainty, A. M., Toksoz, M. N., 1981. Lunar seismology - the
596 internal structure of the moon. J. Geophys. Res. B86, 5061–5074.

597 Goins, N. R., Lazarewicz, A. R., 1979. Martian seismicity. Geophys. Res.
598 Lett. 6, 368–370.

599 Golombek, M. P., Banerdt, W. B., Tanaka, K. L., Tralli, D. M., 1992. A
600 prediction of Mars seismicity from surface faulting. Science 258, 979–981.

601 Goto, A., Taniguchi, H., Yoshida, M., Ohba, T., Oshima, H., 2001. Effects
602 of explosion energy and depth to the formation of blast wave and crater:
603 Field explosion experiment for the understanding of volcanic explosion.
604 Geophys. Res. Lett. 28, 4287–4290.

605 Hartmann, W. K., 2005. Martian cratering 8: Isochron refinement and the
606 chronology of Mars. Icarus 174, 294–320.

607 Hartmann, W. K., 2007. Martian cratering 9: Toward resolution of the con-
608 troversy about small craters. Icarus 189, 274–278.

609 Havskov, J., Alguacil, G., 2004. Instrumentation in Earthquake Seismology.
610 Springer, Netherlands.

611 Holsapple, K. A., Housen, K. R., 2007. A crater and its ejecta: An interpre-
612 tation of Deep Impact. Icarus 187, 345–356.

613 Holsapple, K. A., Housen, K. R., Schmidt, R. M., Wauchope, C.,
614 2003. Explosive and impact crater database. (available online at
615 `http://keith.aa.washington.edu/craterdata/`).

Holsapple, K. A., Schmidt, R. M., 1982. On the scaling of crater dimensions .2. impact processes. J. Geophys. Res. 87, 1849–1870.

Horedt, G. P., Neukum, G., 1984. Comparison of 6 crater-scaling laws. Earth Moon And Planets 31, 265–269.

Ide, S., Beroza, G. C., 2001. Does apparent stress vary with earthquake size? Geophys. Res. Lett. 28, 3349–3352.

Kanamori, H., 1977. Energy-release in great earthquakes. J. Geophys. Res. 82, 2981–2987.

Kawai, K., Takeuchi, N., Geller, R. J., 2006. Complete synthetic seismograms up to 2 Hz for transversely isotropic spherically symmetric media. Geophys. J. Int. 164, 411–424.

Khan, A., Connolly, J. A. D., Maclennan, J., Mosegaard, K., 2007. Joint inversion of seismic and gravity data for lunar composition and thermal state. Geophys. J. Int. 168, 243–258.

Khan, A., Mosegaard, K., Rasmussen, K. L., 2000. A new seismic velocity model for the Mono from a Monte Caril inversion of the Apollo lunar seismic data. Geophys. Res. Lett. 27, 1591–1594.

Knapmeyer, M., Oberst, J., Hauber, E., Wahlisch, M., Deuchler, C., Wagner, R., 2006. Working models for spatial distribution and level of Mars' seismicity. J. Geophys. Res. 111, E11006.

Latham, G., Ewing, M., Dorman, J., Press, F., Toksoz, N., Sutton, G.,

Meissner, R., Duennebi, F., Nakamura, Y., Kovach, R., Yates, M., 1970a. Seismic data from man-made impacts on the moon. Science 170, 620–626.

Latham, G. V., McDonald, W. G., Moore, H. J., 1970b. Missile impacts as sources of seismic energy on the moon. Science 168, 242–245.

Lognonne, P., 2005. Planetary seismology. Annual Review Of Earth And Planetary Sciences 33, 571–604.

Lognonne, P., Beyneix, J. G., Banerdt, W. B., Cacho, S., Karczewski, J. F., Morand, M., 1996. Ultra broad band seismology on InterMarsNet. Plan. & Space Sci. 44, 1237–1249.

Lognonne, P., Gagnepain-Beyneix, J., Chenet, H., 2003. A new seismic model of the Moon: implications for structure, thermal evolution and formation of the Moon. Earth Planet. Sci. Let. 211, 27–44.

Lognonne, P., Giardini, D., Banerdt, B., Gagnepain-Beyneix, J., Mocquet, A., Spohn, T., Karczewski, J. F., Schibler, P., Cacho, S., Pike, W. T., Cavoit, C., Desautez, A., Favede, M., Gabsi, T., Simoulin, L., Striebig, N., Campillo, M., Deschamp, A., Hinderer, J., Leveque, J. J., Moatagner, J. P., Rivera, L., Benz, W., Breuer, D., Defraigne, P., Dehant, V., Fujimura, A., Mizutani, H., Oberst, J., 2000. The NetLander very broad band seismometer. Plan. & Space Sci. 48, 1289–1302.

Lognonne, P., Le Feuvre, M., Johnson, C. L., Weber, R. C., 2009. Moon meteoritic seismic hum: Steady state prediction. J. Geophys. Res. 114, E12003.

Malin, M. C., Edgett, K. S., Posiolova, L. V., McColley, S. M., Dobrea, E. Z. N., 2006. Present-day impact cratering rate and contemporary gully activity on Mars. Science 314, 1573–1577.

Mayeda, K., Walter, W. R., 1996. Moment, energy, stress drop, and source spectra of western United States earthquakes from regional coda envelopes. J. Geophys. Res. B101, 11195–11208.

McGarr, A., Latham, G. V., Gault, D. E., 1969. Meteoroid impacts as sources of seismicity on the Moon. J. Geophys. Res. 74, 5981–5994.

Melosh, H. J., 1980. Cratering mechanics - observational, experimental, and theoretical. Annual Review Of Earth And Planetary Sciences 8, 65–93.

Melosh, H. J., 1989. Impact cratering - a geological process. Vol. 11 of Oxford Monographs on Geology and Geophysics. Oxford University Press.

Mocquet, A., 1999. A search for the minimum number of stations needed for seismic networking on Mars. Plan. & Space Sci. 47, 397–409.

Moore, H. J., Baldwin, R. B., 1968. Ranger VIII and gravity scaling of Lnar craters. Science 159, 333–334.

Mueller, R. A., Murphy, J. R., 1971. Seismic characteristics of underground nuclear detonations 1. seismic spectrum scaling. Bull. Seism. Soc. Am. 61, 1675–1692.

Nakamura, Y., 1976. Seismic energy transmission in lunar-surface zone determined from signals generated by movement of lunar rovers. Bull. Seism. Soc. Am. 66, 593–606.

Nakamura, Y., 1983. Seismic velocity structure of the Lunar mantle. J. Geophys. Res. B88, 677–686.

Nakamura, Y., Koyama, J., 1982. Seismic-Q of the Lunar upper mantle. J. Geophys. Res. B87, 4855–4861.

Nordyke, M. D., 1962. An analysis of cratering data from desert alluvium. J. Geophys. Res. 67, 1965–1974.

Oberst, J., Nakamura, Y., 1987. Distinct meteoroid families identified on the Lunar seismograms. J. Geophys. Res. 92, E769–E773.

Okal, E. A., Anderson, D. L., 1978. Theoretical-models for Mars and their seismic properties. Icarus 33, 514–528.

Patton, H. J., Walter, W. R., 1993. Regional moment - magnitude relations for earthquakes and explosions. Geophys. Res. Lett. 20, 277–280.

Peterson, J., 1993. Observations and modeling of seismic background noise. U.S. Geol. Surv. Tech. Rept. 93-322, 1–95.

Pike, W. T., Standley, I. M., Banerdt, W. B., Mar. 2005. A high-sensitivity broad-band seismic sensor for shallow seismic sounding of the Lunar regolith. In: S. Mackwell & E. Stansbery (Ed.), 36th Annual Lunar and Planetary Science Conference. Vol. 36 of Lunar and Planetary Inst. Technical Report. p. 2002.

Pomeroy, P. W., 1963. Long period seismic waves from large, near-surface nuclear explosions. Bull. Seism. Soc. Am. 53, 109–149.

Popova, O., Nemtchinov, I., Hartmann, W. K., 2003. Bolides in the present and past martian atmosphere and effects on cratering processes. Meteoritics & Planet. Sci 38, 905–925.

Press, W. H., Flannery, B. P., Teukolsky, S. A., Vetterling, W. T., 1992. Numerical Recipes, 2nd Edition. Cambridge Univ. Press, Cambridge UK.

Prieto, G. A., Shearer, P. M., Vernon, F. L., Kilb, D., 2004. Earthquake source scaling and self-similarity estimation from stacking P and S spectra. J. Geophys. Res. B109, B08310.

Quantin, C., Mangold, N., Hartmann, W. K., Allemand, P., 2007. Possible long-term decline in impact rates - 1. Martian geological data. Icarus 186, 1–10.

Richardson, J. E., Melosh, H. J., Artemeiva, N. A., Pierazzo, E., 2005. Impact cratering theory and modeling for the Deep Impact mission: From mission planning to data analysis. Space Sci. Rev. 117, 241–267.

Sato, H., Taniguchi, H., 1997. Relationship between crater size and ejecta volume of recent magmatic and phreato-magmatic eruptions: Implications for energy partitioning. Geophys. Res. Lett. 24, 205–208.

Schmidt, R. M., Housen, K. R., 1987. Some recent advances in the scaling of impact and explosion cratering. Int. J. Impact Eng. 5, 543–560.

Shearer, P. M., 2009. Introduction to Seismology, 2nd Edition. Cam. Univ. Press, Cambridge.

723 Shoemaker, E. M., 1983. Asteroid and comet bombardment of the earth.
724 Annual Review Of Earth And Planetary Sciences 11, 461–494.

725 Sleep, N. H., 1994. Martian plate tectonics. J. Geophys. Res. E99, 5639–5655.

726 Sohl, F., Schubert, G., Spohn, T., 2005. Geophysical constraints on the
727 composition and structure of the Martian interior. J. Geophys. Res. 110,
728 E12008.

729 Sohl, F., Spohn, T., 1997. The interior structure of Mars: Implications from
730 SNC meteorites. J. Geophys. Res. E102, 1613–1635.

731 Stein, S., Wysession, M., 2002. An Introduction to Seismology, Earthquakes
732 and Earth Structure. Wiley-Blackwell.

733 Stevenson, D. J., 2001. Mars' core and magnetism. Nature 412, 214–219.

734 Takeuchi, N., Geller, R. J., Cummins, P. R., 1996. Highly accurate P-SV
735 complete synthetic seismograms using modified DSM operators. Geophys.
736 Res. Lett. 23, 1175–1178.

737 Walker, J. D., 2003. Loading sources for seismological investigations of as-
738 teroids and comets. Int. J. Impact Eng. 29, 757–769.

739 Whitaker, E. A., 1972. Photogeology: Part I. Artificial lunar impact craters
740 photographed by Apollo 16. Apollo 16 Preliminary Science Report NASA
741 SP-315, 29.39–29.44.

742 Yoder, C. F., Konopliv, A. S., Yuan, D. N., Standish, E. M., Folkner, W. M.,
743 2003. Fluid core size of Mars from detection of the solar tide. Science 300,
744 299–303.

745 Zharkov, V. N., Gudkova, T. V., 1997. On the dissipative factor of the Mar-
746 tian interiors. Plan. & Space Sci. 45, 401–407.

Quantity	Value	Fractional error			Contribution to fractional error σ_M/M		
$\mathbf{D} = aE^b$							
a	8.8×10^{-3}	$\frac{\sigma_a}{a}$	=	0.35	$\frac{1}{bd}\frac{\sigma_a}{a}$	=	0.9
b	0.32	$\frac{\sigma_b}{b}$	=	0.03	$\frac{1}{b^2 d}\ln\left[\frac{D}{a}\left(\frac{g}{g_\oplus}\right)^{\frac{3}{16}}\right]\frac{\sigma_b}{b}$	=	2.0†
$\mathbf{E}_s = kE$							
k	2×10^{-5}	$\frac{\sigma_k}{k}$	=	10	$\frac{1}{d}\frac{\sigma_k}{k}$	=	8.0
$\mathbf{E}_s = cM^d$							
c	4.8×10^{-9}	$\frac{\sigma_c}{c}$	=	0.49	$\frac{1}{d}\frac{\sigma_c}{c}$	=	0.4
d	1.24	$\frac{\sigma_d}{d}$	=	0.01	$\frac{1}{d^2}\ln\left[\left(\frac{D}{a}\left(\frac{g}{g_\oplus}\right)^{\frac{3}{16}}\right)^{\frac{1}{b}}\frac{k}{c}\right]\frac{\sigma_d}{d}$	=	0.2†
					Total σ_M/M		8.3

Table 1: Contribution to the $M(D)$ error budget from the different derived quantities used in this paper. Error expressions were derived from the error propagation formulae in Bevington and Robinson (1992). The total fractional error σ_M/M, obtained by assuming independence of each error source and summing the variances, is of order 8 (around one order of magnitude in M for a given D). The error in seismic efficiency is the largest contributor to the overall error budget. †Calculated assuming a representative value of D=50 m.

E_{min} (J)	E_{max} (J)	M (Nm)		M_W		Diameter (m)	(m)	N (per year)	N_{min} (per year)	N_{max} (per year)
10^8	10^9	2.3×10^9	1.5×10^{10}	0.2	0.7	3.67	7.64	482	300	1240
10^9	10^{10}	1.5×10^{10}	9.3×10^{10}	0.7	1.2	7.64	15.8	121	65.5	316
10^{10}	10^{11}	9.3×10^{10}	6.0×10^{11}	1.2	1.8	15.8	33.0	19.1	9.15	70.6
10^{11}	10^{12}	6.0×10^{11}	3.8×10^{12}	1.8	2.3	33.0	68.6	2.30	1.09	9.98
10^{12}	10^{13}	3.8×10^{12}	2.4×10^{13}	2.3	2.9	68.6	143	0.280	0.130	1.19
10^{13}	10^{14}	2.4×10^{13}	1.6×10^{14}	2.9	3.4	143	297	0.0321	0.0140	0.142
10^{14}	10^{15}	1.6×10^{14}	1.0×10^{15}	3.4	3.9	297	617	0.00298	0.00118	0.0153
10^{15}	10^{16}	1.0×10^{15}	6.4×10^{15}	3.9	4.5	617	1280	0.000220	0.000085	0.00130
10^{16}	10^{17}	6.4×10^{15}	4.1×10^{16}	4.5	5.0	1280	2660	0.000018	0.000010	0.000094
10^{17}	10^{18}	4.1×10^{16}	2.6×10^{17}	5.0	5.5	2660	5540	0.0000042	0.0000027	0.0000106

Table 2: Number of impact events N expected in each energy range E_{min}–E_{max}. N_{min} and N_{max} give the minimum and maximum number of events based on uncertainties in the $D(E)$ relation. Equivalent seismic moments M and moment magnitudes M_w are calculated using the relations given in the main text.

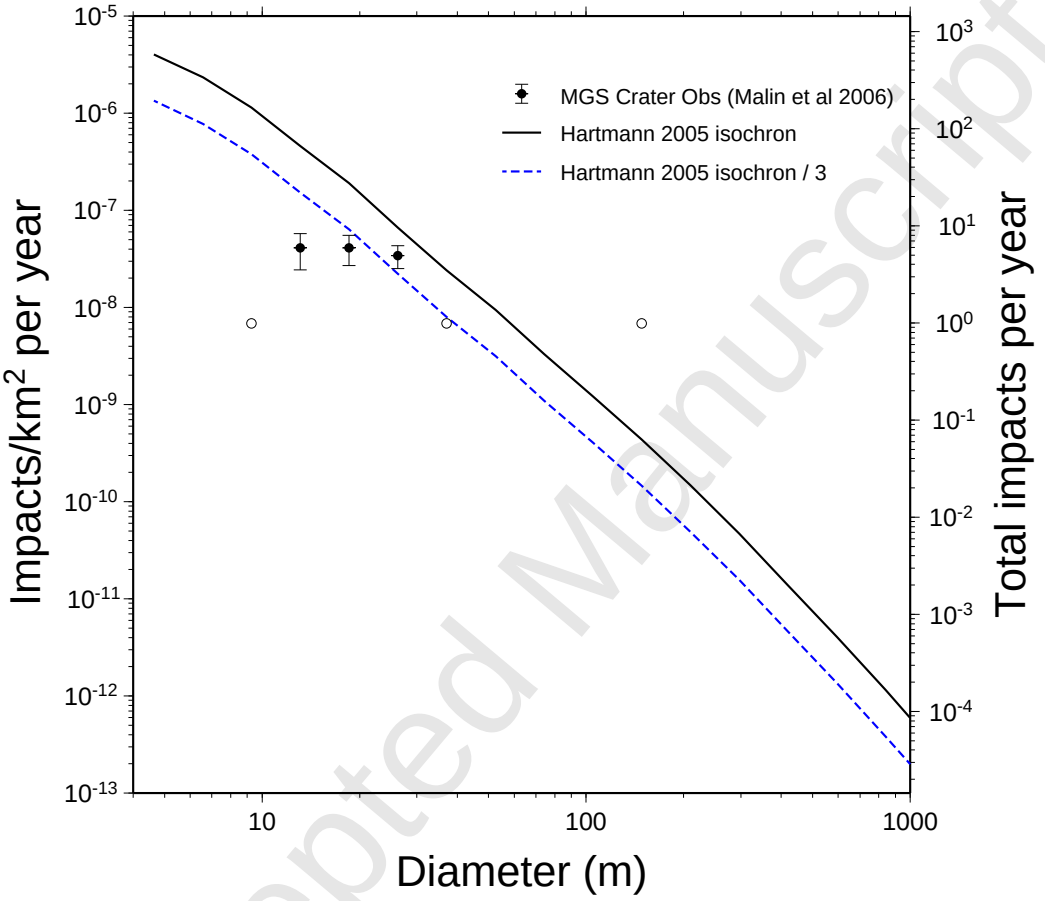

Figure 1: Cratering 1-year isochron for Mars extrapolated from the Hartmann (2005) 3 Gyr isochron compared to measurements of new craters observed by Malin et al. (2006). The observed recent cratering suggests a correction factor of 1/3 must be applied to the Hartmann (2005) isochron for recent small craters. The bins defining the isochrons are the same as those used by Hartmann (2005), i.e. they give the number of craters per year in diameter intervals that are evenly spaced in $\log_{10}$(diameter) by $0.5 \log_{10} 2$ (e.g. 10–14.1 m, 14.1–20 m, 20–28.3 m, etc). Open/solid symbols contain single/multiple crater measurements respectively.

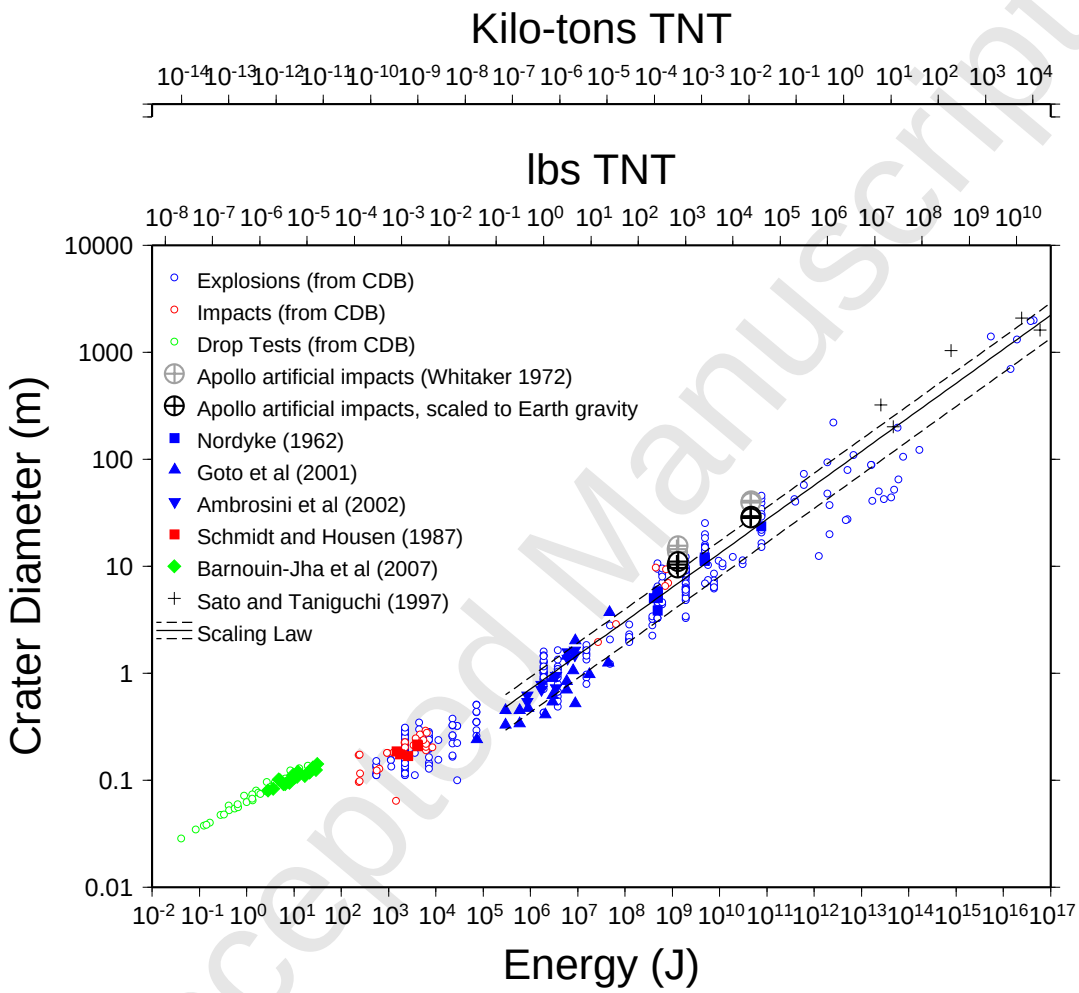

Figure 2: Measurements of crater diameter as a function of impact energy taken from the cratering database (CDB) of Holsapple et al. (2003) augmented with additional and post-1998 measurements. The solid and dashed lines show our derived scaling law and uncertainty bounds. Low energy ($E < 10^5$J) impacts/explosions and drop tests are not representative of the meteorite impacts considered in this study and were not included when calculating the scaling law.

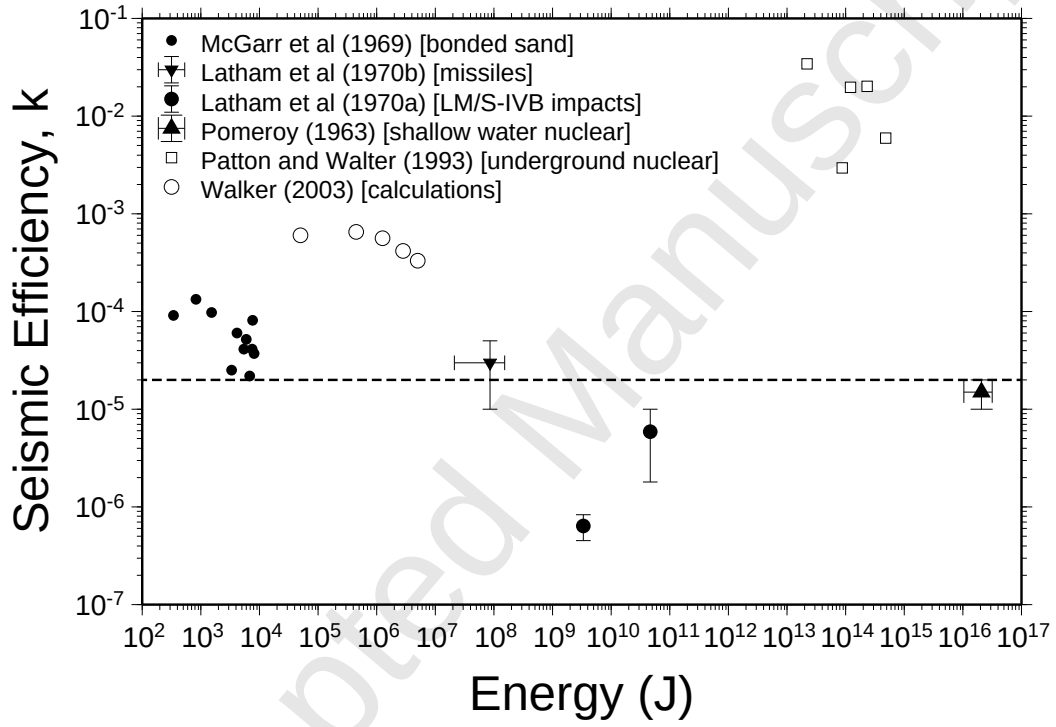

Figure 3: Seismic efficiency as a function of source energy compiled from various studies. The data are very scattered, indicating the large uncertainty in k. The dashed line shows our adopted value of k=2×10^{-5}, which is broadly consistent (within an order of magnitude) with most of the experimental data. The k values for underground nuclear explosions are much higher and are not representative of impact processes.

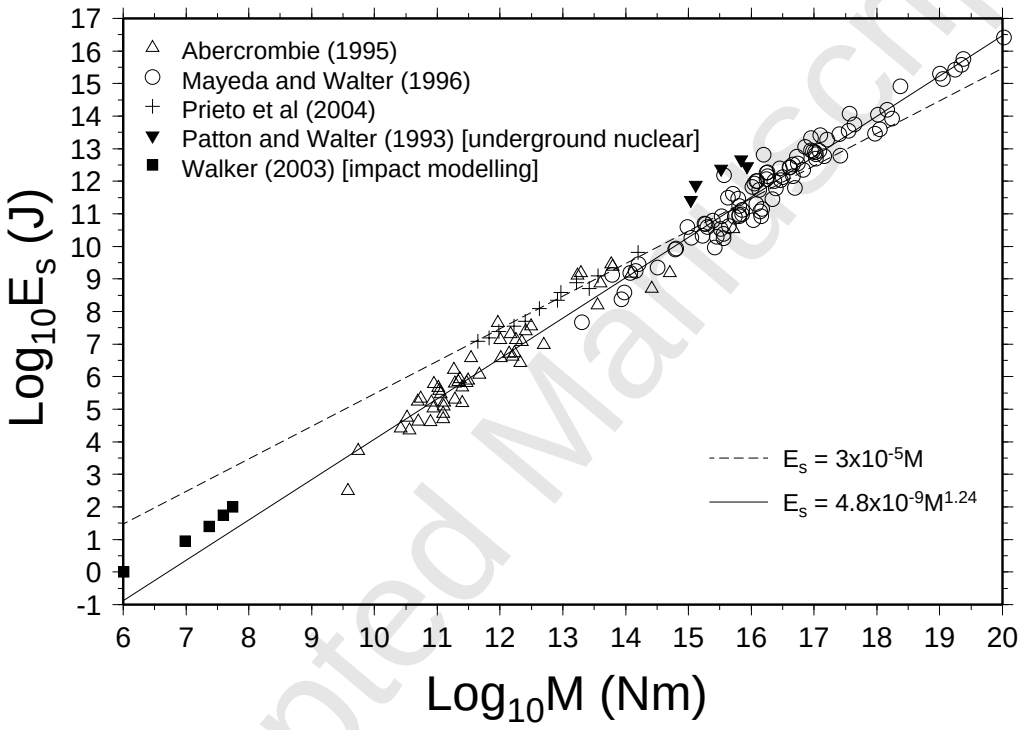

Figure 4: Relationship between seismic moment and total radiated seismic energy. Data are from regional studies of small earthquakes (Abercrombie, 1995; Mayeda and Walter, 1996; Prieto et al., 2004), impact modelling (Walker, 2003), and nuclear explosions (Patton and Walter, 1993). The trend lines are shown from Ide and Beroza (2001) (dashed line) and this study (solid line). The $E_s = 4.8 \times 10^{-9} M^{1.24}$ trend fits these regional results the best and is considered most relevant to the present study.

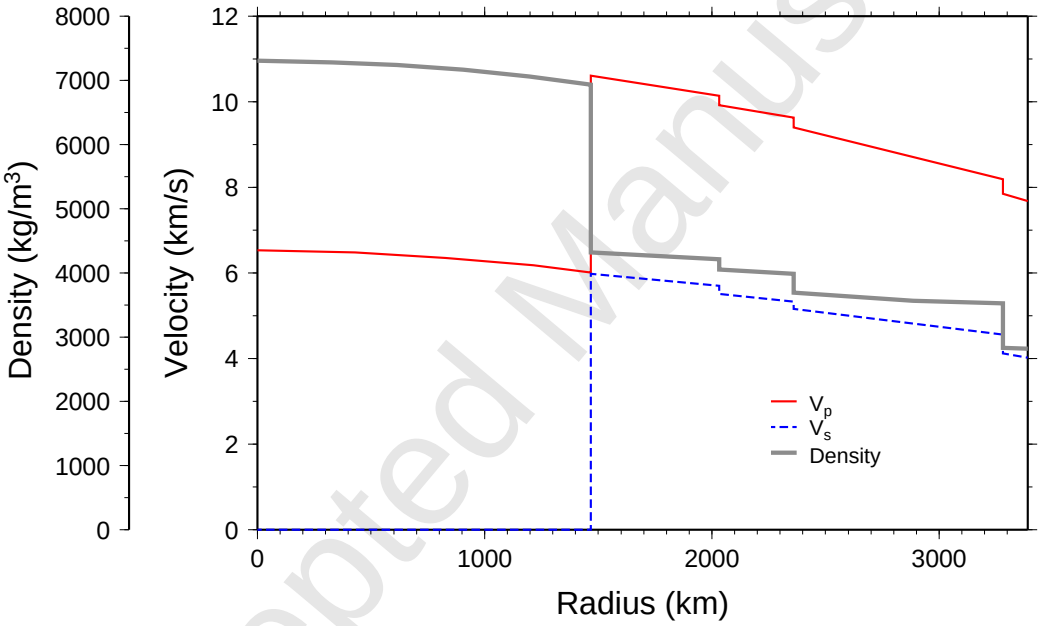

Figure 5: Seismic velocity and density model for Mars from Sohl and Spohn (1997) (Model A).

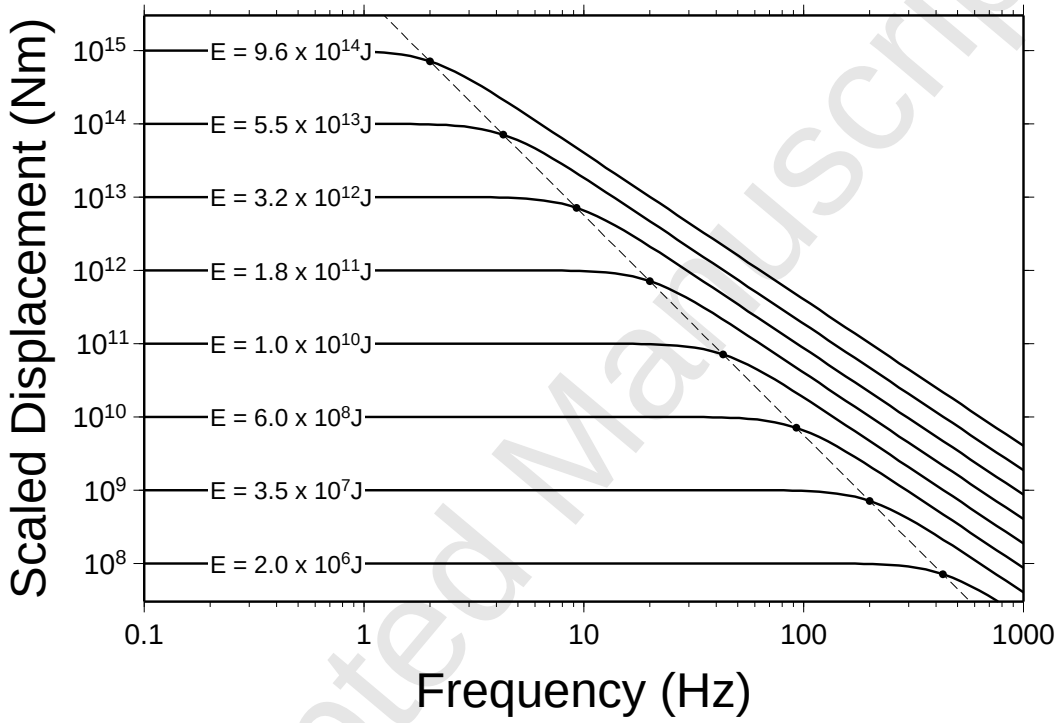

Figure 6: Seismic displacement source spectra used for creation of the synthetic seismograms scaled by the seismic moment. The equivalent impact energy E is given for each case. Source spectra are essentially flat below 4 Hz for all but largest events. Hence, at teleseismic distances the high frequency content will be determined primarily by attenuation along the ray-path for all but the largest impacts. Spots and dashed line show the corner frequencies f_c which follow a f^{-3} trend. Frequency fall off above f_c follows a standard f^{-2} law.

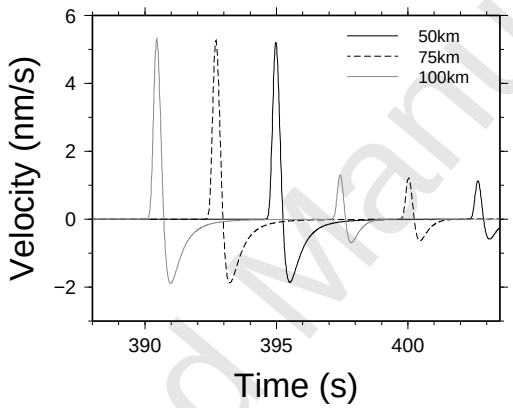

Figure 7: Synthetic seismograms for a M=10^{14} Nm event generated with 8 Hz maximum frequency and source depths of 50, 75, and 100km for a source-receiver offset of 60°. The difference between body wave amplitudes (P-waves in this plot) for different source depths is negligible and can be accounted for by slight differences in geometrical spreading. Therefore, while it is not computationally feasible to model surface events using DSM, a 50km source depth will give representative body wave amplitudes.

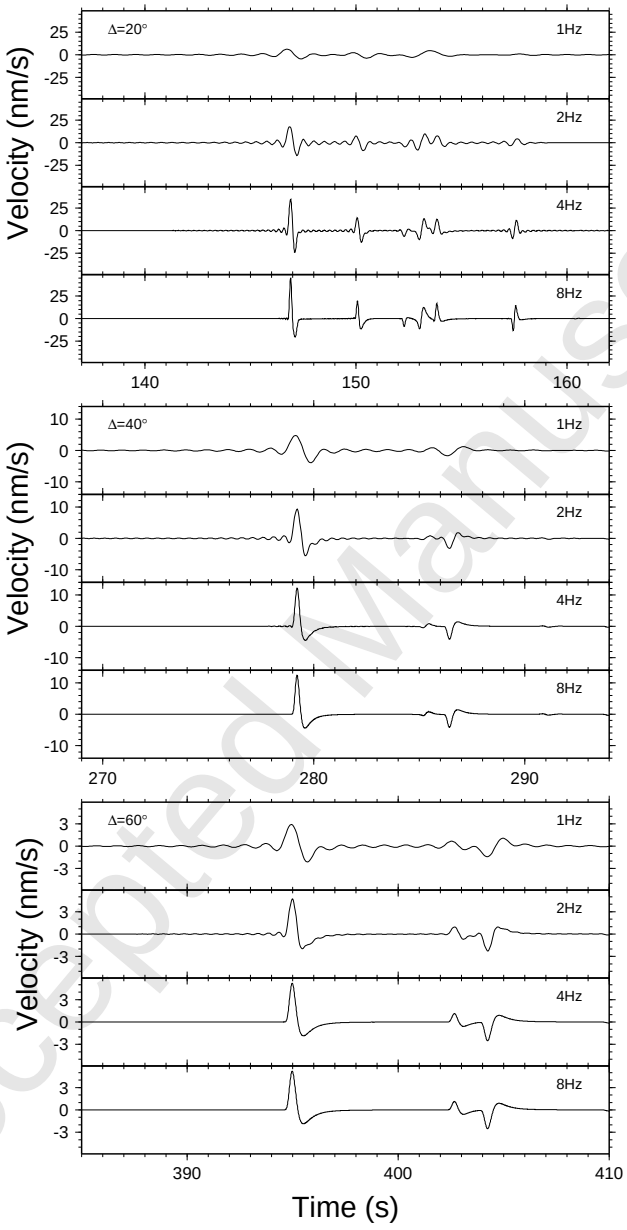

Figure 8: Waveforms for 1, 2, 4, and 8 Hz maximum modelled frequencies at source-receiver offsets Δ of 20, 40 and 60° for an event with M=10^{14} Nm. Note that more distant events have lower frequency content due to increased seismic attenuation. At Δ=20° some slight ringing is still visible in the 8 Hz model, implying that the synthetics have not quite converged at these small offsets.

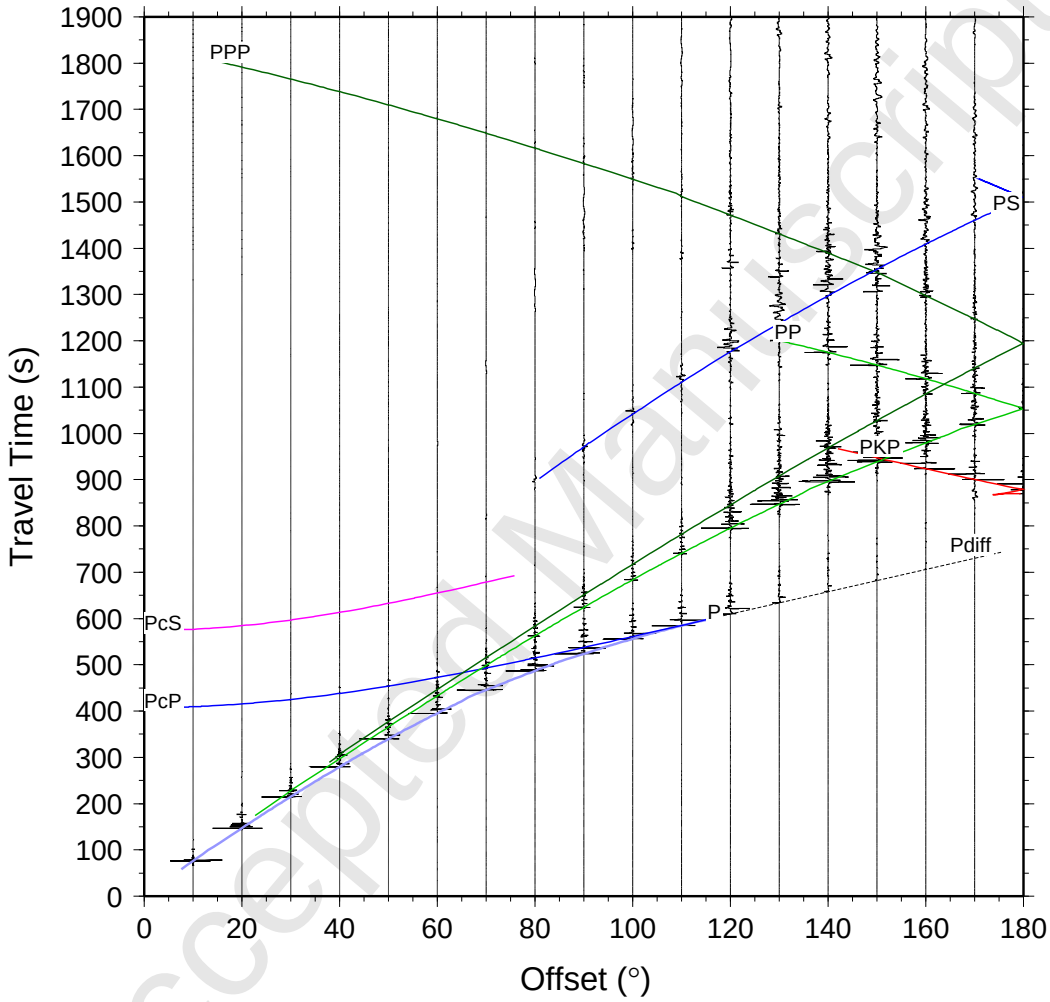

Figure 9: Record section compiled from synthetic seismograms over a full Martian hemisphere. Travel time curves calculated using the Tau-P toolkit (Crotwell et al., 1999) for various phases generated using an isotropic source are also shown. A P-wave shadow zone exists beyond Δ=110°.

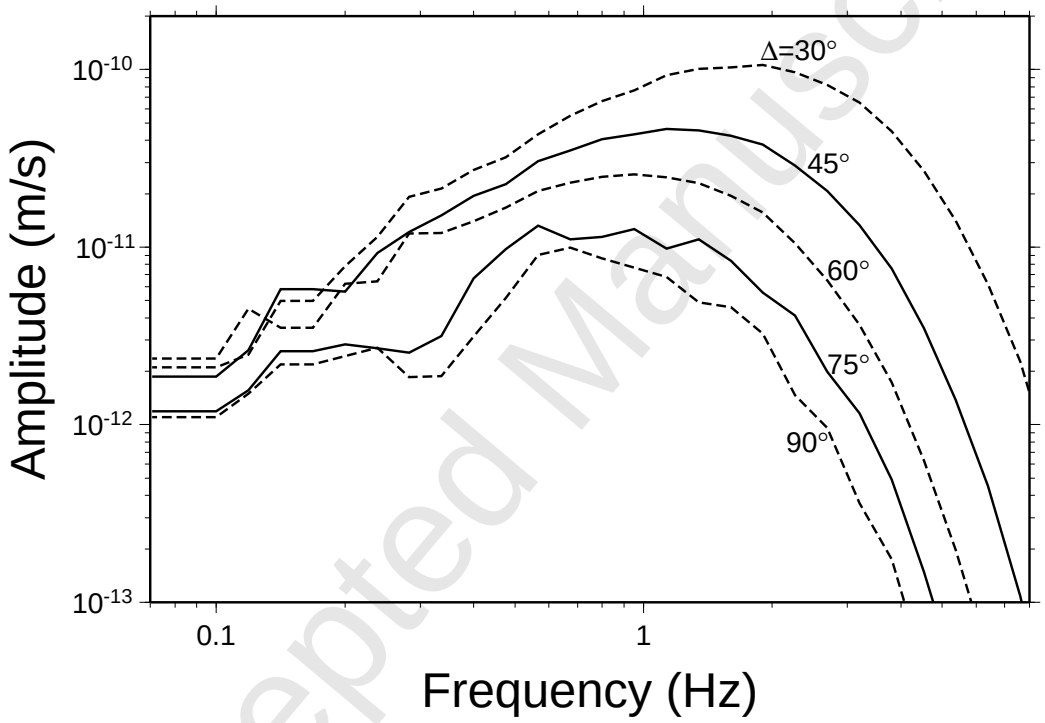

Figure 10: Spectra of P-wave envelope for a range of source-receiver offsets Δ for an event with M=10^{14} Nm. Larger offsets have less high frequency content due to seismic attenuation. Most of the frequency content is in the 0.4–4 Hz range.

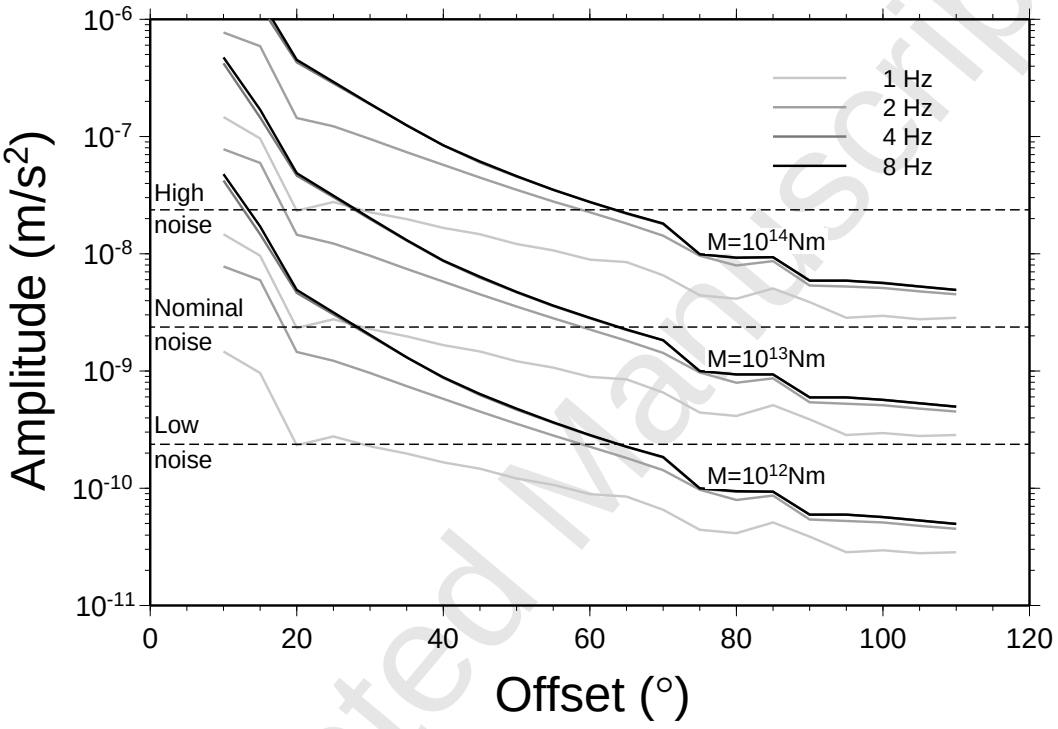

Figure 11: Maximum P-wave amplitude in the frequency range 0.4-4 Hz as a function of source-receiver offset and seismic moment for 8 Hz synthetics. Results from 1, 2, and 4 Hz models are also shown to give an idea of the convergence. Representative noise levels are also shown (dashed lines) over the same spectral range for noise spectral densities of 10^{-10} ms^{-2}Hz$^{-1/2}$ (low noise), 10^{-9} ms^{-2}Hz$^{-1/2}$ (nominal noise), and 10^{-8} ms^{-2}Hz$^{-1/2}$ (high noise). For the nominal noise case a globally detectable event must have a seismic moment of at around 10^{14} Nm (M_w=3.3), and at least 10^{13} Nm (M_w=2.6) to be detectable at 60° offset.

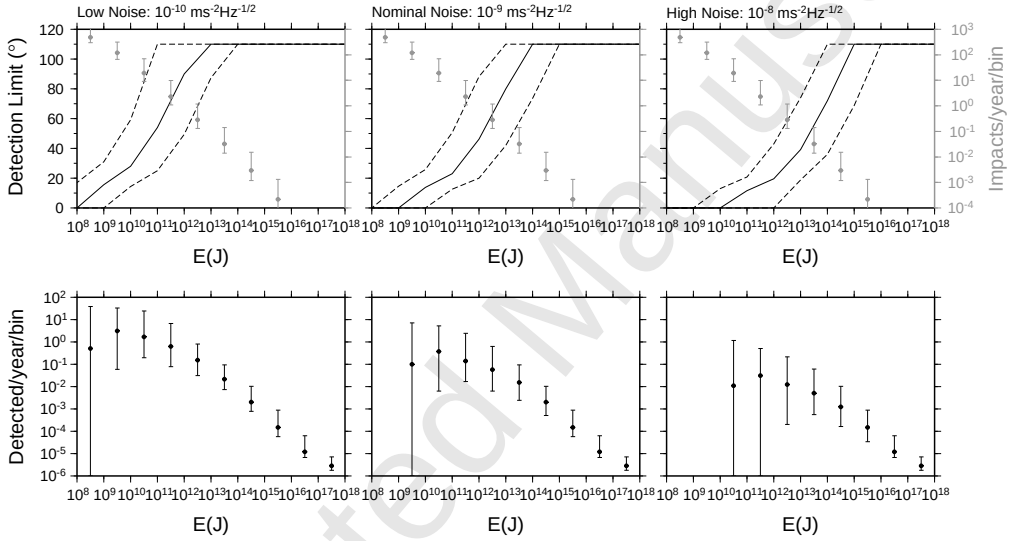

Figure 12: Detectability of meteorite impacts on Mars for deployments with low, nominal, and high noise levels. In the top panels, solid lines and dashed error envelopes show the maximum source-receiver offset where the impact induced seismic signal is above the noise for a given impact energy E. Grey points with errors show the number of impacts over the whole of Mars for each decadal energy bin from Table 2. Lower panels show the resulting number of detectable events per year in each energy bin at a single seismic station.